Article

Numerical Study of the Layered Blasting Effect on a Cemented Backfill Stope

Zongnan Li [1,2], Bin Yu [1,3], Lijie Guo [1,3,*], Wenyuan Xu [1,3], Yue Zhao [1,3] and Xiaopeng Peng [1,3]

1   Beijing General Research Institute of Mining and Metallurgy, Beijing 100160, China
2   School of Civil and Resources Engineering, University of Science and Technology Beijing, Beijing 100083, China
3   National Centre for International Research on Green Metal Mining, Beijing 102628, China
*   Correspondence: guolijie@bgrimm.com

Abstract: The sublevel open stoping with backfill method has recently been widely used in underground metal mines. The primary CPB stope is frequently affected by blasting in the secondary ore stope, leading to stope collapse and ore dilution, which has become a common problem and has received widespread attention. Numerical simulations are carried out in the present work, and a 1/4 numeral model consisting of a primary CPB stope and a secondary ore stope is built. The secondary ore stope is divided into four layers on average in the simulation model, and the incident stress induced by each blasting at the interface of the CPB and ore is simulated. The results show that the CPB stope in the range within the height of the explosive charge induced horizontal compressive stress and tensile stress induced from the explosive charge height, while the mined section under the charge height has no obvious blasting impact. The maximum incident compressive stress is close to 1.2 MPa and occurs in the area closest to the blast hole The maximum induced tensile stress occurs in the range above the charge height, which is about 0.2 MPa. The stress ratios of the four-layered lift blasts are 3.6%, 3.8%, 4.0%, and 4.8%, respectively, showing a slight cumulative effect of layered blasting. In addition, the positive correlation between incident stress and the stress ratio is studied in the present work, and the results show that the greater the incident stress is, the greater the incident ratio is.

Keywords: blasting; cemented paste backfill; peak particle velocity; metal mine; layered blasting

1. Introduction

The sublevel open stoping with backfill method has recently been widely used in underground metal mines [1,2]. It is one of the most important technologies in underground mines due to its high efficiency and safety [3–5]. The main feature of this technology is dividing the primary stope (stopes) and secondary stope (blocks) for mining and filling in turn [6,7]. The primary stope is first blasting-mined and then filled with a backfilling slurry by sequence. The secondary stope mines after the primary stope. The whole stope is divided into several layers in height for blasting, and each layer is blasted and mucked before the next [8,9]. Generally, the height of each blasting layer is in the range of 4–8 m. Once the stope is mined out, the backfill is required. One typical filling material is the mixed slurry of cement, tailings, and water with various proportions [10,11]. After a period of a hydration reaction, the slurry solidifies into solid mass, which can support the surrounding rock and improve the stress field environment [12,13]. The cemented paste backfills (CPB) mass of the primary stope is thus frequently affected by the adjacent ore stope blasting, as shown in Figure 1. A series of problems such as collapse, spalling, support failure, etc. occurred in the CPB stope due to the exposure and vibration induced by lift blasting in the ore stope [14–17]. This is an important problem that affects the high-quality and safe mining process. It has become the key work of filling mechanics research and has been widely dealt with by technicians and researchers [18–21].
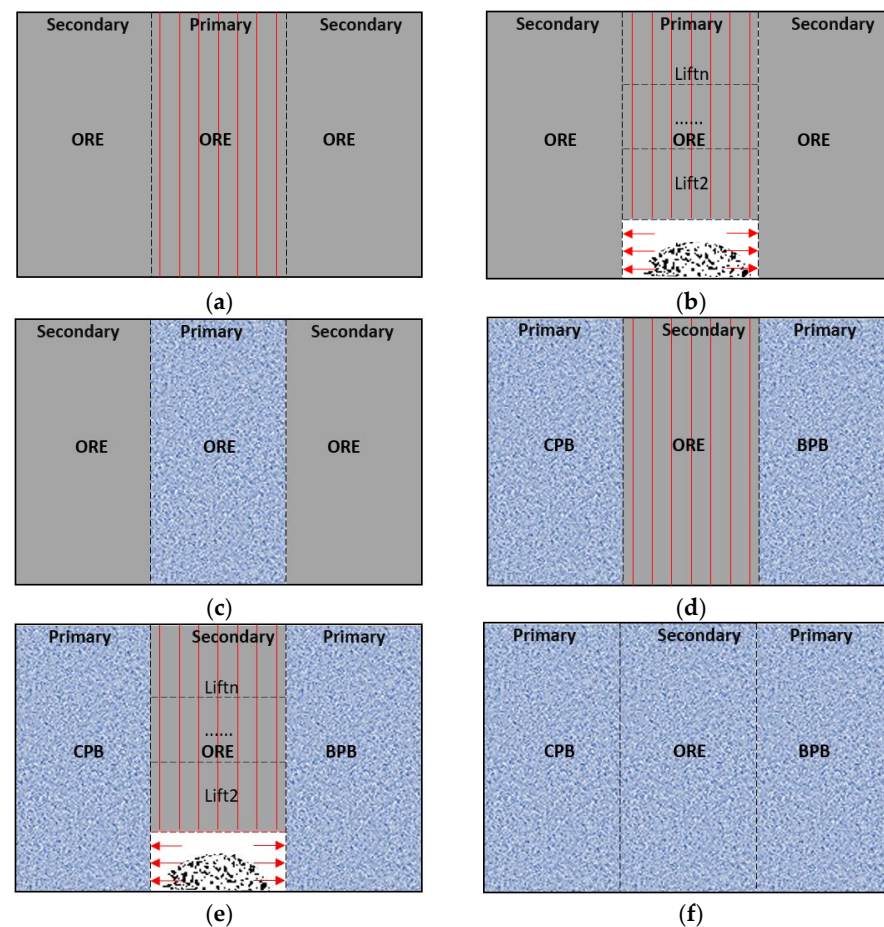
Figure 1. Stope mining and backfill sequence. (**a**) Primary stopes planed; (**b**) Primary stope layer blast; (**c**) Primary stope backfill; (**d**) Secondary stopes planed; (**e**) Secondary stope layer blast; (**f**) Secondary stope backfill.

For the stability analysis method of the filling stope, Mitchell [22] proposed a method considering the stope size and assuming the slip plane for calculating the stability of the CPB stope, which is the application of the limit-equilibrium slip in the backfill mining. Liu et al. [23]. considered the time factor of the cemented backfill stope, analyzed the applicability of the Mitchell method, and believed that the results of the Mitchell solution were closer to the situation under short-term undrained conditions than long-term drainage conditions for the CPB stope. Lili [24–28] proposed a three-dimension wedge failure model and suggested the formula under the different disclosed conditions, which improved and extended the Mitchell method, Peng et al. [29]. proposed a safety factor method to comprehensively evaluate the impact of mining methods and the quality of the fresh filling slurry on the CPB; the strength of the CPB is required and then specified with a factor, which is useful in practice.

The static analysis method still plays a dominant role, and the complex boundary condition model is constantly proposed, which is essentially an extension of the limit equilibrium theory. However, with the development of computing technology, more complex environmental models have been taken into account, in which blasting-induced damage is one of the most important environmental factors [30–33]. Muhammad Emad et al. [34]. built a three-dimension numerical model, applied a dynamic load to simulate the blasting effect to the primary CPB stope, and discovered that failure due to blast vibrations is initiated at the top of the stope in the form of a wedge rather than at the bottom of the stope derived from static limit equilibrium theory. They believed that dynamic modelling is considerably more realistic than traditional static modelling in the failure analysis of CPB stopes. Suazo et al. [35] studied the effects of the blast hole layout and sequencing of

detonation to the stope CPB; the result showed that explosives along a direction parallel to the exposed face of the CPB was the most disadvantageous, with the highest pressure being caused by blasting and the pressure being up to several megapascals at the barricade level, which is much larger than of the static result. Li et al. [36]. built a three-dimension numerical model to simulate the damage of the stope CPB due to an adjacent ore blast; it was found that a low cement-to-sand ratio of CPB with a lower damage influence is beneficial to resisting blasting damage.

It is difficult to find the answer with a simple static mathematic model for the CPB damage induced by the stress wave propagating from the secondary ore stope [37–39]. Numerical simulation is the effective method to research such dynamic load effect [40–42], but due to the difference in engineering geological conditions, the boundary and material parameters for the numerical simulation model are various, so the conclusions are different [43–46]. However, how the stress wave propagates at the non-uniform interface between the ore and the CPB stope and how the layered blasting affects the incident stress in the CPB stope are still unclear and need to be enriched. In the present work, a numerical simulation model consisting of a primary CPB stope and a secondary ore stope is established, and the influence of layered lift blasts on an adjacent CPB stope is analyzed. The height of the model is 24 m, and the plane size is 6 m × 2 m. A typical cylindrical blast hole with a diameter of 160 mm and a length of 24 m is adopted, which is located 2 m away from the CPB stope. Based on the typical two-step mining technology, the stope is mined out by four layered lift blasts. The cumulative effect of lifting blasts on an adjacent CPB is considered, and the incident stress caused by blasting is analyzed It can be a reference for the stability research of CPB stopes.

2. Materials

2.1. Tailings

The tailings for the CPB specimen used in the present study were sourced from a copper mine in south China. Density tests followed the relevant ASTM (American Society for Testing and Materials) guidelines and the National Standards of P.R.C [47], and the results illustrate that the tailings have a specific gravity D_S of 3.20. Particle size distribution (PSD) tests followed ASTM D422-07, and the results show that the tailings below 37 μm and 75 μm in size account for 60.97% and 77.68% respectively. The PSD (particle size distribution) of the tailings is shown in Figure 2.
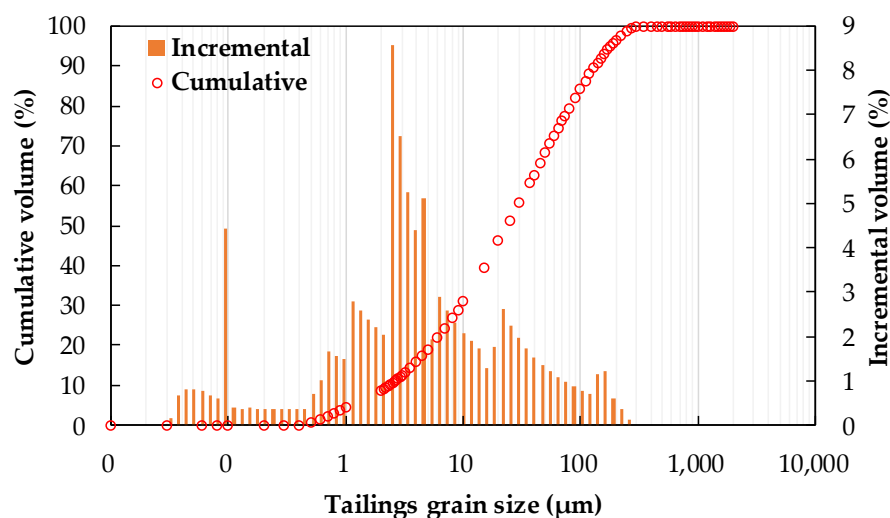

Figure 2. PSD curve of the copper tailings used in the present work. Particles of the size of the tailings below 37 μm and 75 μm account for 60.97% and 77.68% respectively.

The main contents of the tailings material used in this study are silicon dioxide (SiO_2), iron (TFe), calcium oxide (CaO), and aluminum oxide (Al_2O_3), with mass fractions of 15.15%, 7.05%, 11.15%, and 1.93%, respectively, according to the ICP (Inductive Coupled Plasma Emission Spectrometer) analysis in the lab.

2.2. Strength Test

CPB samples are drilled from the bottom of the primary stope; the curing time is more than 60 d. The depth of the sampling hole is 30 m, which is equivalent to 25 m of the stope. Samples are prepared with a column test specimen that is 50 mm × 100 mm (diameter Φ × length L) in size. Uniaxial compression (UC) tests were carried out on CPB specimens using a closed-loop servo-controlled testing machine (Instron-1342, Norwood, MA, USA) with a loading capacity of 500 kN. For an accurate result, the test group consists of three samples, which are tested separately. Another four CPB samples were prepared and subjected to a conventional triaxial compression (CTC) test under four different confining pressure values of 0.2 MPa, 0.3 MPa, 0.4 MPa, and 0.5 MPa by using a 63.5 mm HTC Hoek triaxial cell as the confining apparatus, following the ASTM D2664 standard. The machine loading rate for both the uniaxial and triaxial compression tests was set to 0.1 mm/min.

As the UC test result, the uniaxial compressive strength (UCS) of the CPB sample is 2.0 MPa, the axial deformation rate under the peak stress is 1.2%, the Young's modulus, as determined by the stress–strain relationship curve, is 195.9 MPa, and the measured Poisson's ratio is 0.268. The curves of the deviator stress versus the axial strain of the in situ CPB under four confining pressures were measured, as shown in Figure 3a. The relationship between the principal stresses under the ultimate limit state is summarized in Figure 3b. It is shown that the first principal stress (σ_1) and the third principal stress (σ_3) of the CPB in the failure point are linear. Thus, the cohesion (C) and internal friction angle (φ) were calculated as 41.7° and 0.5 MPa, respectively, based on the Coulomb criterion [48] by Formula (1).
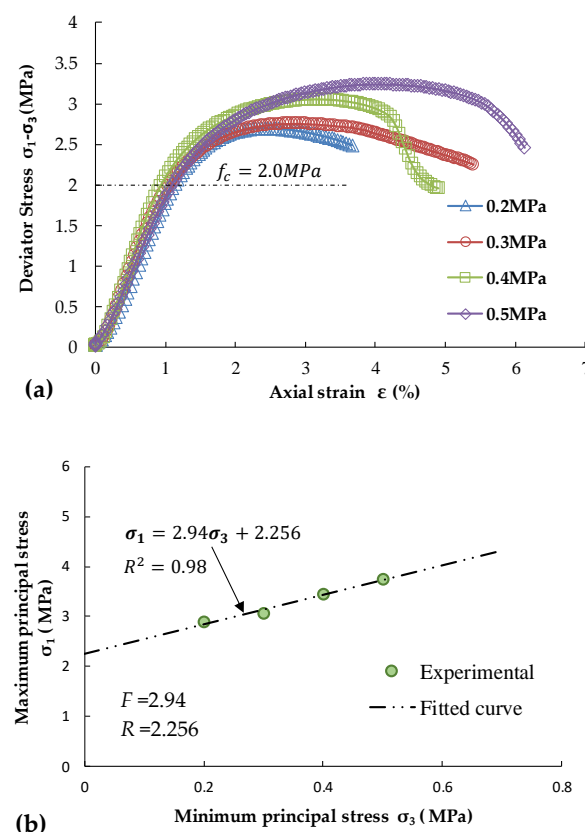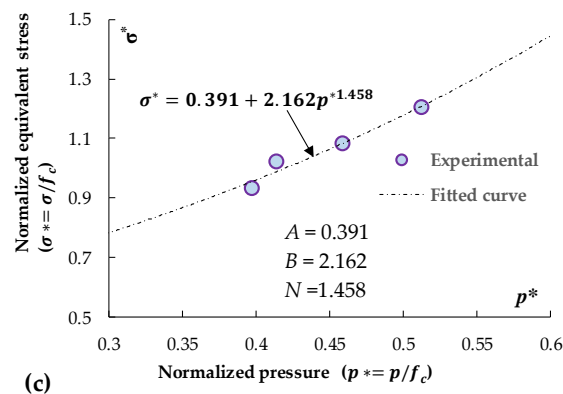

(a)

(b)

Figure 3. *Cont.*

(c)

Figure 3. Relationship curve of stress–strain and the HJC parameters. (**a**) CTC deviator stress–strain curve; (**b**) Fitting curve of the CTC maximum and minimum principal stress relationship; (**c**) Fitting curve of the normalized equivalent stress and normalized pressure relationship.

$$\left.\begin{aligned} \sigma_1 &= F\sigma_3 + R \\ \varphi &= \text{atan}\left(\frac{F-1}{2\sqrt{F}}\right) \\ C &= \frac{R}{2\sqrt{F}} \end{aligned}\right\} \tag{1}$$

where F and R is are the fitting coefficients of the linear relationship between σ_1 and σ_3, and C and φ are the cohesion and internal friction angle.

3. Numerical Modelling

3.1. Method

A 1/4 numeral model consisting of a primary CPB stope and a secondary ore stope is built; the stope is divided into four layers equally, each layer corresponding to one lift blasting. Each ore layer will be deleted before the next lift blast, and the cylinder blast hole is set in the ore stope, 2 m away from the CPB stope. The velocity of nodes is set to zero, and the stress and deformation of the last blast are retained for each lift blast, except for the first blast, as a simulation for the mining process. Figure 4 shows the scheme of the lift blast. The Arbitrary Lagrange-Euler (ALE) algorithm is adopted, in which the explosive and air elements are set as Euler elements to provide the explosive dynamic load. The CPB element, ore element, and stemming elements are set as Lagrange elements and contain its deformation characteristics [49–51].
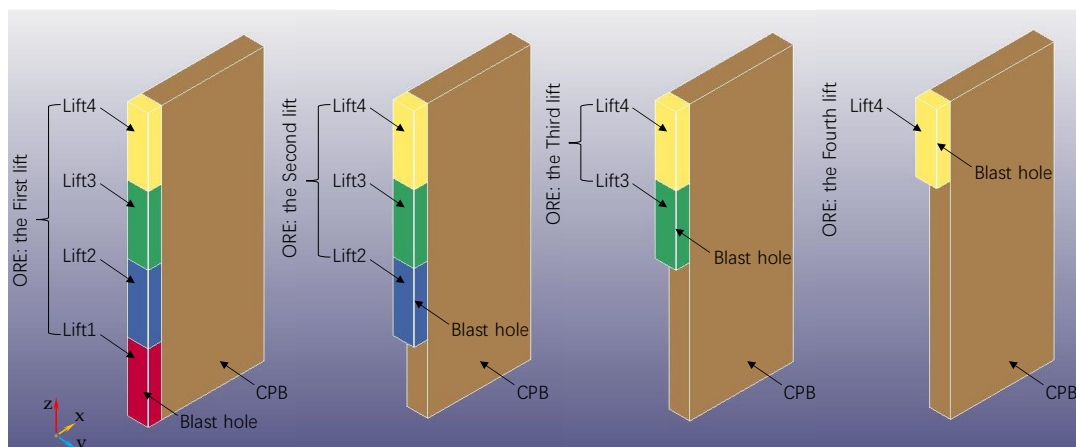

Figure 4. Lift blasting model for the primary stop: Lift 1 to Lift 4 are the ore materials in the secondary stope and will be blasted down in the cut process; the CPB stope is adjacent to the ore stope and will be affected by the explosive blasting in the ore stope.

The calculation time for each lift blast is 20 MS, which is long enough for the explosive detonation process. The time interval is 0.5 MS for each result file, which includes the unit stress, strain, deformation, and other information. Therefore, 40 result files are output for each lift blast. The maximum compressive stress exceeds 200 MPa, the tensile stress exceeds 20 MPa, and the strain exceeds 5% during calculation; the elements fail in the present work [35,44]. Symmetrical boundary conditions are adopted on the symmetrical plane of the model, fixed boundary conditions are adopted at the bottom of the model, free boundary conditions are adopted at the top, and non-reflective boundary conditions are adopted at the outside of the filling body [36]. Additionally, the gravity of the model itself is also considered, with the direction towards the negative Z axis in Figure 4.

3.2. Geometric Model

The total width of the model is 8 m, including the ore stope (2 m width) and CPB stope (6 m width). The diameter of the blast hole is 160 mm and is located on the edge of the model at the ore stope side to simulate the impact of secondary stope blasting on the adjacent CPB stope. The height of each continuous blasting lift layer is 6 m along the height of the model, and four continuous mining blasting layers are set in the height direction. Therefore, the total height of the model is 24 m; each blast consists of 4 m of explosives and 2 m of stemming, which is roughly equivalent to the mine situation. The parameters are shown in Table 1.

Table 1. Geometric model parameter for the lift blast.

Properties		Symbol	Value/Description
Model length (m)		L	8
Model width (m)		W	2
Model height (m)		H	24
Blasting material flow range (a × b) air (m)		a	2
		b	2
Radius of the blast hole (mm)		r	160
Distance of the outer hole to the CPB (m)		s	2
Height of the layered blast (m)		H0	6
Real constants of each region in the model		R1~R15	-
Model part	Null	P1	LAG [1]
	Stem/Null	P2~P5	LAG [1]
	ORE	P6~P9	LAG [1]
	CPB	P10	ALE [2]
	AIRE	P12	ALE [2]
	Explosive/AIRE	P11, P12~P15	ALE [2]
Mode boundary	Lateral surface	N1	SYMM [3]
	Lateral surface	N2	SYMM [3]
	Lateral surface	N3	NB [4]
	Lateral surface	N4	NB [4]
	Bottom surface	N5	FIXED [5]
	Top surface	N6	FREE [6]

1—The element obeyed the Lagrangian formulation; 2—The multi-material element with blank material obeyed the Euler algorithm; 3—The symmetry boundary was used; 4—Non-reflection boundaries were used; 5—All nodes on the surface are fixed; 6—Unconstrained free surfaces.

The mesh size used in the elements of the blast hole is less than 0.1 m, while that used in the ore and CPB was 0.025 m around the blast holes and 0.5 m at the edges. Consequently, a total of 449,940 finite elements were used in the model.

3.3. Material Parameters

3.3.1. CPB

The Holmquist–Johnson–Cook (HJC) mode was used to simulate the behavior of the CPB under the blast loading in this study. The HJC model can describe the strain hardening and strain softening behaviors of concrete-like materials [52,53]. As an elastic-viscoelastic model, the HJC model was widely used in the simulation materials under the conditions of a high strain rate, a large strain, and a high pressure; it has been used to model CPB and rock materials in reported studies [44,54]. The HJC consists of the yield surface, state equation, and damage evolution equation, as follows.

(1) The yield surface is defined by normalized equivalent stress and can be described in Figure 5, as follows [52].
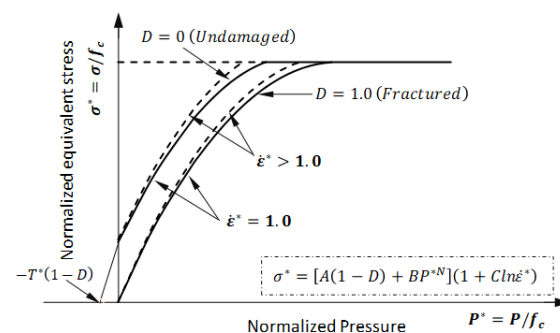

Figure 5. Yield surface curve in the characteristic stress space of the HJC material model.

As shown in Figure 5, the relation between the normalized equivalent stress (Yield surface σ^*) and the normalized pressure (P^*) of the HJC model can be expressed by Equation (2), as follows.

$$\begin{cases} \sigma^*(P^* \geq 0) = \left[A(1-D) + BP^{*N}\right]\left[1 - c\ln\left(\dot{\varepsilon}^*\right)\right] \\ \sigma^*(P^* < 0) = \frac{A}{T^*(1-D)}P^* + A \end{cases} \tag{2}$$

where $\sigma^* = \sigma/f_c$ is the normalized equivalent stress, σ is the actual equivalent stress, and f_c is the uniaxial compressive strength, and the relationship $\sigma^* \leq S_{\max}$ is adopted, where $S_{\max}$ is the normalized maximum strength, $P^* = P/f_c$ is the normalized pressure, $\dot{\varepsilon}^* = \dot{\varepsilon}/\dot{\varepsilon}_0$ is the dimensionless strain rate, $\dot{\varepsilon}$ is the actual strain rate, and $\dot{\varepsilon}_0$ is the reference strain rate ($\dot{\varepsilon}_0 = 1.0s^{-1}$). A, B, N, and $S_{\max}$ are the constants of the yield strength surface. The yield surface parameters are usually obtained by testing without considering the strain rate.

(2) The damage of the HJC model is accumulated by the plastic strain, including the equivalent plastic strain and volume strain, which can be described in Figure 6 [52].
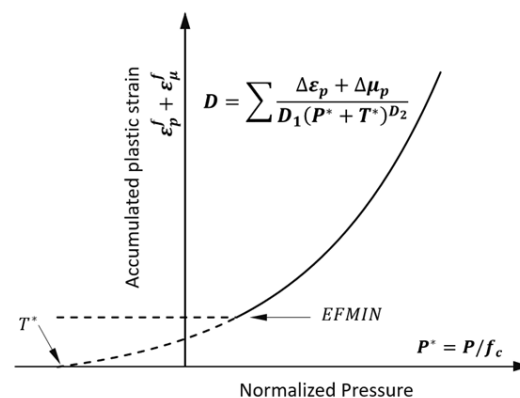

Figure 6. Damage evolution in the stress–strain space of the HJC material model.

$EFMIN$ is the minimum plastic strain in Figure 6. The damage variable (D) in the HJC model is defined as follows.

$$D = \sum \frac{\Delta\varepsilon_p + \Delta\mu_p}{\varepsilon_p^f + \mu_p^f} \tag{3}$$

$$\varepsilon_p^f + \mu_p^f = D_1(P^* + T^*)^{D_2} \tag{4}$$

where $\Delta\varepsilon_p$ and $\Delta\mu_p$ are the equivalent plastic strain and the plastic volumetric strain in one integration circle, and D_1 and D_2 are the material damage constants. In the original literature, the recommended values were 0.04 and 1.0.

(3) The relationship between the volumetric strain and the pressure of materials is described by the equation of state. The equation of state of the HJC model consists of three parts: elastic compression, compaction deformation, and deformation after compaction, respectively, as shown in Figure 7 [52].
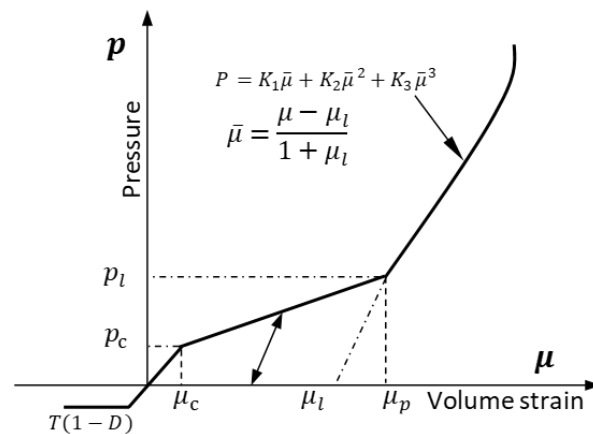

Figure 7. EOS curve of the HJC model in various stress stages.

In the deformation after compaction part, the pores of the material are fully compacted, and plastic deformation occurs. The EOS can be written as follows.

$$\begin{cases} p_{load} = k_1\overline{\mu} + k_2\overline{\mu}^2 + k_3\overline{\mu}^3 \\ \quad p_{unload} = k_1\overline{\mu} \end{cases} \tag{5}$$

where k_1, k_2, and k_3 are material constants and can be obtained by the Hugoniot test data. p_{crush}, p_{lock}, and μ_{lock} are obtained as follows.

$$p_{crush} = f_c/3 \tag{6}$$

$$\mu_{crush} = \mu_{crush}/K \tag{7}$$

$$\rho_{lock} = \rho_g/\rho_0 - 1 \tag{8}$$

where K is the bulk modulus, ρ_g is the compacted density, ρ_0 is the density, $\rho_g = \rho_0/(1-q)$, and q is the Porosity. Unlike rock materials or high-strength concrete materials, which can take an impact force up to hundreds of megapascals, the peak impact load of filling materials is generally a few megapascals or tens of megapascals [15,55]. Therefore, the literature value of CPB materials is referenced in the present work [56].

The sensitivity of HJC parameters was analyzed in the literature [57]. These include Uniaxial compressive strength (f_c), Bulk modulus (K), Normalized cohesive strength (A), Normalized pressure hardening (B), Pressure hardening exponent (N), and Locking volumetric strain (μ_l). B, N, G, and μ_{lock} are highly sensitive to the results, while other parameters are generally sensitive. Therefore, parameters with a strong sensitivity in the

HJC model have been supplemented following the method proposed by [58,59]. These parameters used in the present work are from the CTC test results, as shown in Figure 3c, As a comparison, Table 2 shows the HJC model parameters used in this study and those of the original concrete materials.

Table 2. Parameters of the HJC materials used in the present work.

Parameter		Concrete [52]	CPB	ORE
Mass density, ρ_0 $\left(\text{kg}\cdot\text{m}^{-3}\right)$		2440	2000	3200
Shear modulus, G (GPa)		14.86	0.085	13.89
Quasi-static UCS, f_c (MPa)		48	3.2	60
Normalized cohesive strength, A		0.79	0.391	0.55
Normalized pressure hardening, B		1.60	2.162	1.23
Pressure hardening exponent, N		0.61	1.458	0.76
Strain rate coefficient, C		0.007	0.007	0.0097
Normalized maximum strength, $S_{\max}$		7	2	7
Maximum tensile hydrostatic pressure, T (MPa)		4	0.6	4.0
Damage constant	D_1	0.04	0.04	0.04
	D_2	1.0	1.0	1.0
Crushing pressure, P_{crush} (MPa)		16	1.0	20
Locking pressure, P_{lock} (MPa)		800	80	800
Crushing volumetric strain, μ_{crush}		0.001	0.0075	0.00125
Locking volumetric strain, μ_{lock}		0.1	0.10	0.174
Amount of plastic strain before fracture, $EF_{\min}$		0.01	0.01	0.01
Pressure constant	K_1 (GPa)	85	85	39
	K_2 (GPa)	−171	−171	−233
	K_3 (GPa)	208	208	550

3.3.2. Ore

The HJC materials model is also used in the simulation of ore material, the UCS of ore mass is about 60 MPa, the density is 3.2×10^3 kg/m³, the Young's modulus and the Poisson's ratio are 13.89 GPa and 0.21, respectively, by test results in the lab [47], the HJC parameters were from the literature [13,44], with similar strengths as a simplification, and the parameters are shown in Table 2.

3.3.3. Explosive

The explosive material model can be expressed by the Jones–Wilkens–Lee (JWL) equation of state (EOS) function; EOS gives the relationship between the pressure and detonation volume, as follows:

$$P = A\left(1 - \frac{\omega}{R_1 V}\right)e^{-R_1 V} + B\left(1 - \frac{\omega}{R_2 V}\right)e^{-R_2 V} + \frac{\omega E_0}{V} \tag{9}$$

where P is the explosive pressure; V is the relative volume; E_0 is the initial internal energy; A, B, R_1, and R_2 are material constants; and ω is the Grüneisen constant. In this paper, The values of these can be found in the literature [18]. Here, the high energy emulsion explosive with a density of $1.63 \times 10^3/\text{m}^3$ is used, the explosive pressure is 16 GPa, and the detonation velocity is 6690 m/s, according to the product description [9].

3.3.4. Other Materials

Drilling chips or sand are often used as hole-stemming materials for mining blasting in the stope. Therefore, solid kind materials are used to model the stemming materials referenced in the literature [9,60]. Here, the density of materials is 1.7×10^3 kg/m^3, the Shear modulus is 2.524 MPa, the Bulk modulus is 4673 MPa, and the material will fail when the strain exceeds 10% in this work. Null material is used in the present work to simulate air materials with a density of 1.29 kg/m^3; this material model is expressed by a linear polynomial equation of state and can be used to simulate ideal gas [9].

4. Result and Discussion

4.1. Effect of Blasting Scenarios in the CPB Stope

The explosive detonates in the ore stope, 2 m away from the CPB stope. The blasting stress wave passes through the ore mass and penetrates the CPB mass, inducing the stress changes in the CPB stope. The impact effect on the CPB stope is first formed on the contact boundary interface (heterointerface of rock and cemented backfill: HRCB) of the two materials and gradually propagates into the CPB stope. Figure 8 plots the distribution of von Mises stress in the CPB stope induced by the lift blasting.

The first lift layer is 6 m in height, and the length of the charge is 4 m, as shown in Figure 8a. The blasting is started at 0 MS, and 20 MS of evolution time is recorded, where six time points (2 MS, 4 MS, 8 MS, 10 MS, 15 MS, 20 MS) are selected to better display the evolution process of the blasting results. The maximum von Mises stress generated on the CPB is about 0.5 MPa, which occurred on the HRCB about 2 ms after blasting, extending about 8 MS to the total HRCB. The influence on the height direction of the CPB is greater than that on the horizontal direction, and the influence effect on the range of the blast hole height is greater than that beyond the blast hole height. In addition, in the direction of stress wave propagation, the horizontal stress changes alternately in tension and compression.

Before the second lift blast, the elements of the first lift blast layer in the ore stope are deleted, and the velocities of all the model elements are set to zero, as a simulation of the actual mining process. The duration of the secondary lift blast record is also 20 MS, and the blasting source distance and charge amount are consistent with the first lift blasting. As shown in Figure 8b, stress waves appear on the HRCB at about 2 MS, with a maximum von Mises stress of 1.0 MPa, and stress waves expand all of the HRCB at about 8 MS. The stress in the height direction of the CPB is greater than that in the horizontal direction, and stress in the range of the blast hole height is greater than that of the range in the non-blast hole height; in particular, stress and deformation are not obvious between the non-contact part below the charge height.

Before the third lift blast, elements in the ore stope of the secondary lift layer were deleted; the height range is 6 m to 12 m, as shown in Figure 8c. Similarly, the nodes' velocities of all the elements in the model were set to zero, as a simulation of the mining process. The duration time of the third lift blast is set to 20 MS, and the blasting charge structure and explosive charge amount are unchanged compared to the last blast. It can be seen that the stress wave propagation features are roughly consistent with the last blast. The stress wave is generated at the HRCB at about 2 MS, with a maximum equivalent stress of 1.1 MPa, and then conducted to the interior of the CPB stope. The stress within the range of the explosive charge height is higher than that in other areas and is not obvious for the blasted areas.

Figure 8d shows the result of the fourth lift blast. The explosive detonated after the ore elements of the third lift blast layer were deleted, that is, the ore elements within the range of 12 m to 18 m were deleted, and the node velocities of all the elements were reset to zero consistency with the previous initialization. The recording time was also 20 MS, and other information remained unchanged. It should be pointed out that the top surface of the CPB model was free, which will have little effect on the result of the fourth lift blasting. It can be seen that stress is generated on the HRCB surface at 2 MS and with a maximum equivalent

stress of 1.3 MPa. For the last blasting, the CPB stope located within the charging height between 18 m and 24 m has obvious stress but little stress below 18 m.
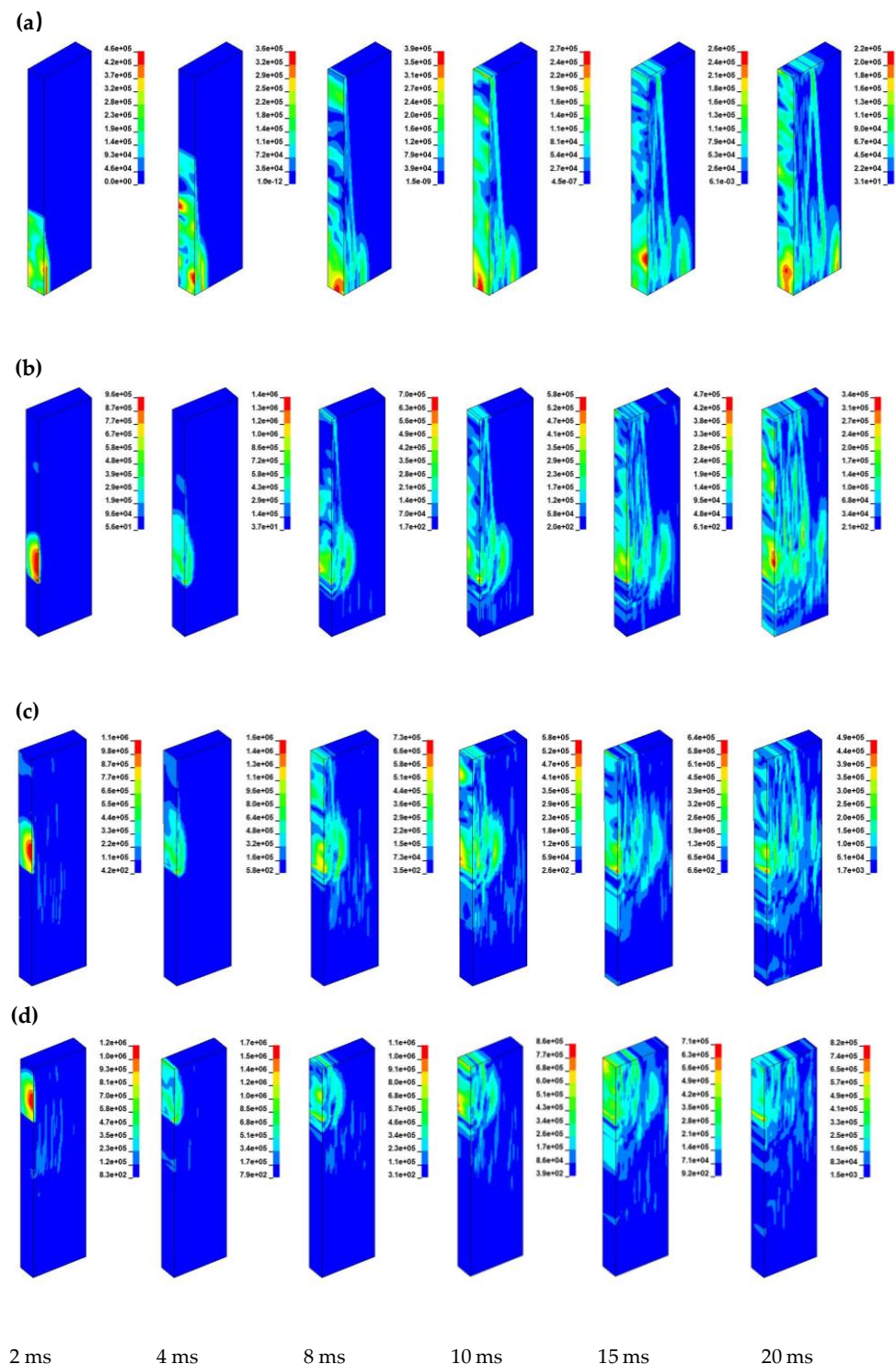

Figure 8. Stress evolution in the CPB stope induced by blasting in an adjacent ORE stope: (**a**) the first lift blast; (**b**) the secondary lift blast; (**c**) the third lift blast; (**d**) the fourth lift blast.

The evolution characteristics of the stress nephogram in the fourth lift blast show that the peak value appears in the range of the charge height at the initial stage for each blasting, which occurred at about 2 MS after initiation. The maximum stress value of blasting appears in the fourth lift blast, reaching 1.3 MPa.

4.2. Incident Stress

The lateral horizontal impact stress produced by the blasting stress wave is an important factor for the stability of the CPB stope. The collapse of the CPB stope often occurs near HRCB, which is an important factor of dilution loss in the two-step filling mining method. A 24 m-high path is selected along the HRCB interface in the model. The horizontal stress values at 2 MS, 6 MS, 12 MS, and 18 MS along the path are picked from the computed result file marked as S1, S2, S3, and S4 in Figure 9.

Figure 9a shows the first lift blast results. It can be seen that the horizontal stress has experienced the vibration process of increasing and decreasing the compressive stress and increasing and decreasing the tensile stress. The maximum compressive stress is about 0.8 MPa, which occurs at the bottom of the model, and the maximum tensile stress is about 0.1 MPa, which occurs almost in the full path range. It can also be seen that the range of explosive charge height, i.e., 0–6 m, is dominated by compressive stress.

Figure 9b shows the characteristics of the horizontal stress of the second lift blast. Similar to the previous blasting, the maximum compressive stress zone occurs within the height range of the explosive charge, i.e., 6–12 m. In addition, the tensile stress distribution occurred above the blast height, i.e., above 12 m, and the maximum tensile stress is about 0.2 MPa, which indicates that the layered blasting has formed an obvious tensile stress zone in the area above the explosive charge height.

Figure 9c shows the third blast feature. Compared with the last blast, no obvious horizontal stress growth is found. The maximum compressive stress occurs within the height range of explosive charge, i.e., 12–18 m. which is close to 1.2 MPa, while the maximum tensile stress occurred within the range above the explosive charge height up to 0.2 MPa. Like before, there was no obvious horizontal stress effect below the explosive charge height. The results show that the ore stope blasting produces an obvious compressive stress zone in the CPB stope near the blasting source, an obvious tensile stress zone above the charge height, and no obvious effect in the blasted area below the charge height in the CPB stope.

Figure 9d shows the fourth blast feature. The maximum compressive stress occurs within the height range of the explosive charge height, i.e., 18–24 m; 1.25 MPa is the highest on record, while the maximum tensile stress occurred within the range near the explosive charge height, which is about 0.1 MPa. It can be seen that, within the height range of the first and second lift blasting, it is far away from the blasting source, the ore and rock are not in contact with the backfill body, and the horizontal stress of the CPB elements does not change significantly, which fully shows that the lift blasting has no significant impact on the CPB stope in the mined section.

In general, the layered lift blasting in the ORE stope will have the following effects on the adjacent CPB stope: (a) In the area within the height of the explosive charge in the CPB stope which is closest to the blasting source, there appeared obvious horizontal compressive stress; (b) The tensile stress zone is generated in the CPB stope at a certain distance from the explosive charge; (c) There is no obvious blasting effect for the mined section under the charge height in the CPB stope.

4.3. Stress Ratio

The blasting stress wave passes through the ore materials and propagates to the HRCB in a very short time. Due to the huge properties difference between the two materials, the stress wave reflects and transmits at the HRCB. The stress wave transmitted into the CPB stope and induced the stress changes in a very short time; the changes may induce damage in some area of the CPB stope. Induced stress in the CPB stope is closely related to the blasting energy, and the amplitude of transmission energy can be characterized by the relative change in stress on both sides of the interface. We choose the effective stress contrast between the ore elements and the CPB element on both sides of the boundary for preliminary analysis. The observation point is located on the path along the height direction on the HRCB interface. The lift blast layer is 6 m in height, and 20 observation points are equidistant and set on the path corresponding to each blasting. The result is shown in Figure 10, where four time points (2 MS, 6 MS, 12 MS, 18 MS) are selected for comparison.
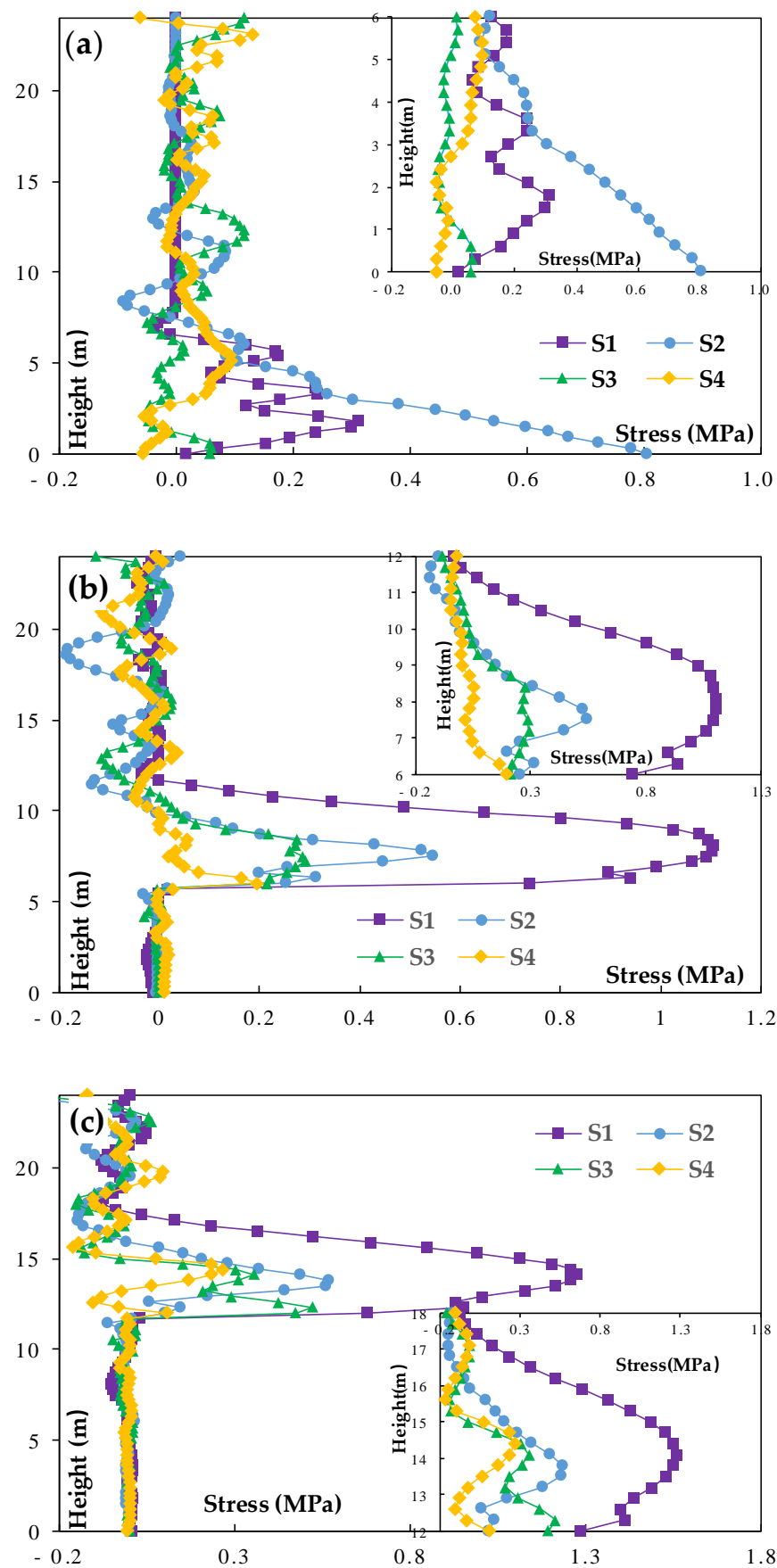
Figure 9. *Cont.*
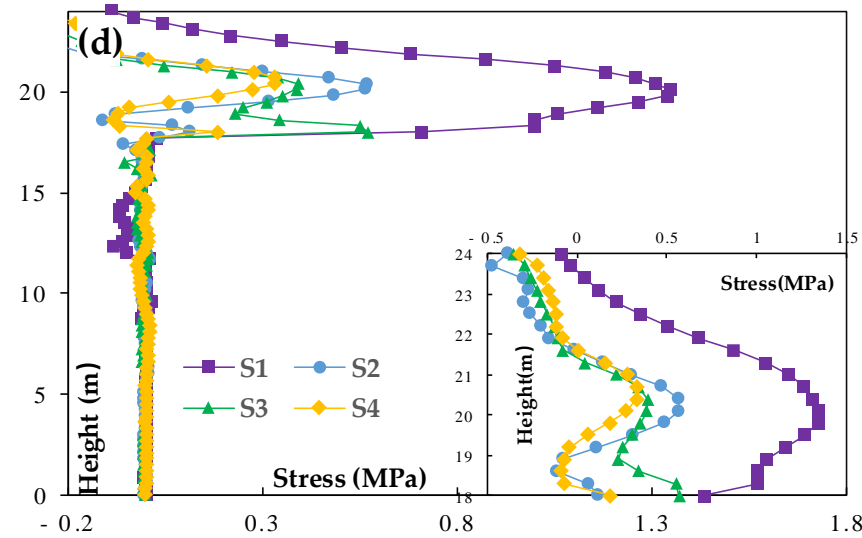
Figure 9. Stress evolution in the CPB stope induced by blasting in an adjacent ore stope: (**a**) the first lift blast; (**b**) the secondary lift blast; (**c**) the third lift blast; (**d**) the fourth lift blast.

The von Mises stresses of the ore and CPB elements at the observation points are compared in Figure 10 for each lift blast. von Mises stress is equivalent to stress based on shear strain energy, and its form is as follows [48]:

$$\overline{\sigma} = \sqrt{\frac{(\sigma_1 - \sigma_2)^2 + (\sigma_2 - \sigma_3)^2 + (\sigma_3 - \sigma_1)^2}{2}} \tag{10}$$

where $\overline{\sigma}$ is von Mises stress, and $\sigma_i (i = 1, 2, 3)$ is the first, second, and third principal.

The stress ratio is defined as follows in Formula (11):

$$SR = \frac{1}{N} \sum_{n=1}^{N} \left(\frac{1}{M} \sum_{m=1}^{M} R_m \right)_n \tag{11}$$

where SR is the stress ratio; it is the average for all observation points at different times on the path. R_m is the stress ratio of the CPB element to the ore element. Here, the stress on the CPB side is considered as the incident stress (IS), and the subscript m represents the number of the points taken. The upper limit of accumulation M represents the total number of points; here, $M = 20$, that is, 20 stress points are taken along the path, with a spacing of 0.3 m. The counting index n represents the time history number, and the upper limit N represents the total number of time histories taken. Here, time histories are selected, i.e., n = 1, 2, 3, and 4 represent 2 MS, 6 MS, 12 MS, and 18 MS, respectively.

In Figure 10a, 2 MS, 6 MS, 12 MS, and 18 MS of von Mises stress in the computed results file for the first lift blasting are selected. By defining Formula (11), the average stress ratios of 2 MS, 6 MS, 12 MS, and 18 MS are 4.7%, 4.0%, 3.2%, and 2.6%, respectively. It can be seen that the stress of the ore element is much greater than that of the CPB element.

In Figure 10b, the stress of the ore elements and CPB elements in the second lift blast is compared at 2 MS, 6 MS, 12 MS, and 20 MS. The results show that the stress of the ore element is also much greater than that of the CPB element, and the stress ratios of 2 MS, 6 MS, 12 MS, and 18 MS are 6.4%, 3.3%, 2.6%, and 2.9% respectively. The overall average stress ratio is 3.8% according to Formula (11). Similarly, the stress comparison of the third and fourth lift blast of the CPB and ore elements is shown in Figure 10c,d. The stress results of 2 MS, 6 MS, 12 MS, and 18 MS are analyzed according to Formula (11), and the results are summarized in Table 3. It can be seen that the stress ratios of the first-, second-, third-, and fourth-layer lift blasts are 3.6%, 3.8%, 4.0%, and 4.8% respectively, and the stress ratios increase slightly with the increase in the blast sequence.
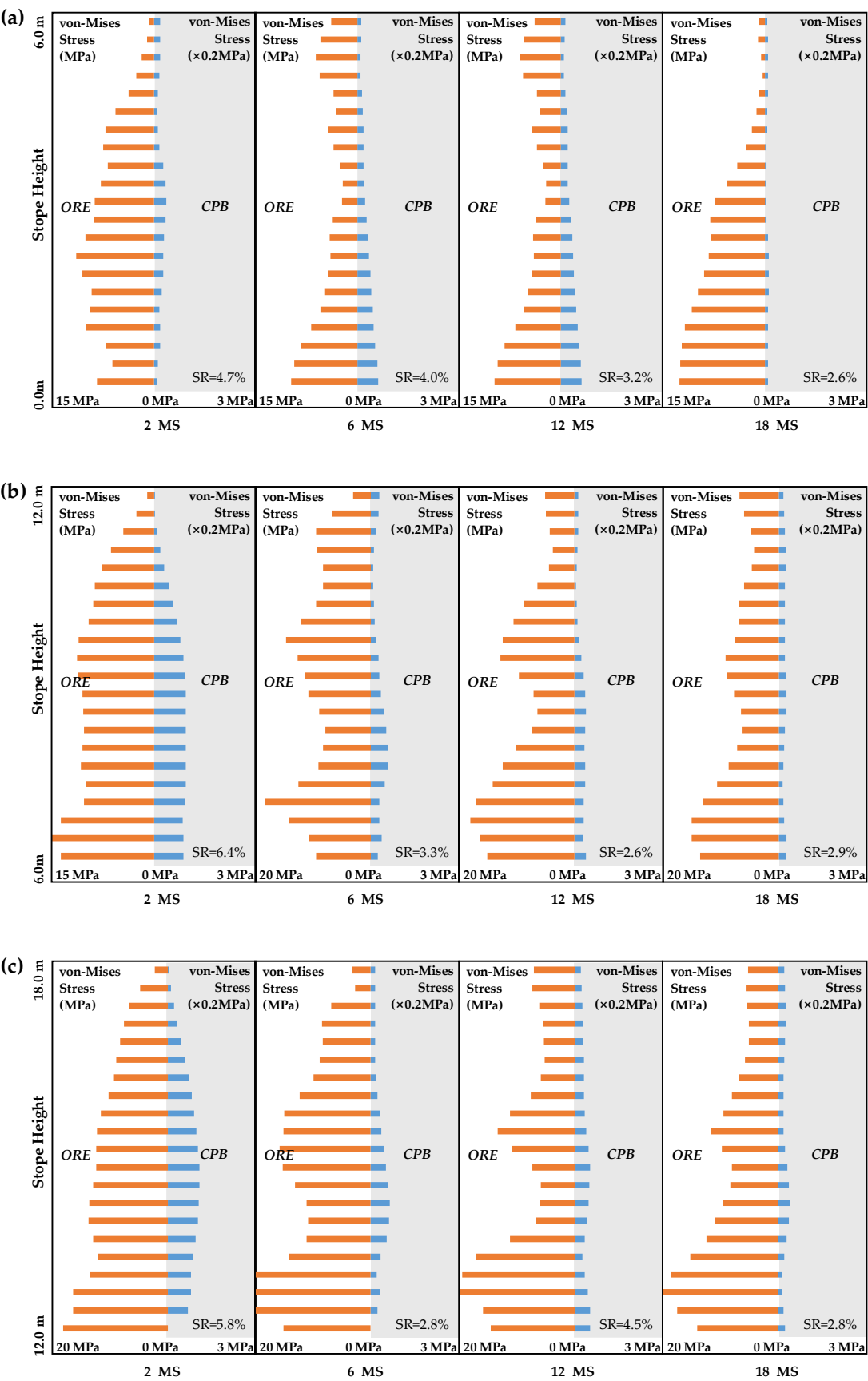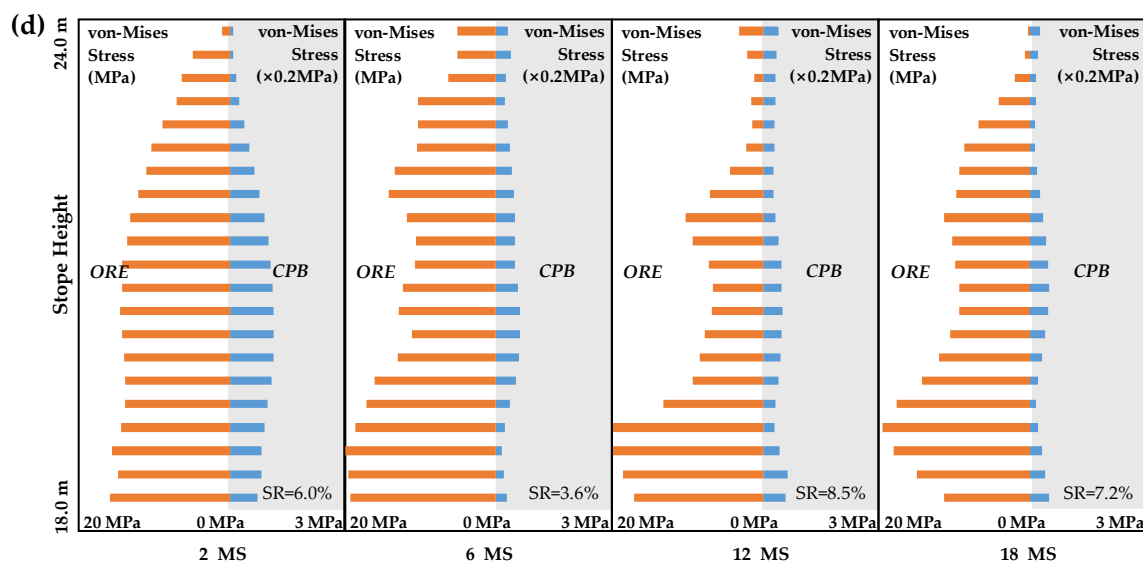
Figure 10. *Cont.*

Figure 10. Equivalent stress ratio of ORE and CPB on HRCB: (**a**) the first lift blast; (**b**) the secondary lift blast; (**c**) the third lift blast; (**d**) the fourth lift blast. Yellow is the von Mises stress of the ore element, blue is the von Mises stress of the CPB element at the corresponding position, and the stress bar of the CPB element is magnified by five times for observation.

Table 3. Statistical results of the layered lift blasting stress ratio.

Blasting Scenarios	Height	Stress Ratio at Different Times				Average Stress Ratio (SR)
		2 MS	6 MS	12 MS	18 MS	
First lift	0~6 m	4.7%	4.0%	3.2%	2.6%	3.6%
Secondary lift	6~12 m	6.4%	3.3%	2.6%	2.9%	3.8%
Third lift	12~18 m	5.8%	2.8%	4.5%	2.8%	4.0%
Fourth lift	18~24 m	6.0%	3.6%	4.5%	5.1%	4.8%

Data on the observation path for the four-layered lift blast are selected, and the relationship between the incident stress (IS) and the stress ratio (SR) is compared, as shown in Figure 11a. At the same time, the stress ratio distribution under different incident stresses is counted, and the results are summarized as shown in Figure 11b. It can be seen from Figure 11a that the incident stress at the initial stage of blasting (about 2 MS) is the maximum, about 0.6~1.2 MPa, and the corresponding stress ratio is in the range of 4~10%. The incident stress decreases after the peak impact stress (after 2 MS), and the corresponding incident stress ratio also decreases to less than 6%. We divide the incident stress level into the following categories: a low stress level, that is, the incident stress is less than or equal to 0.4 MPa; a high stress level, that is, the incident stress is greater than 0.8 MPa; and a medium stress level, which is between 0.4 MPa and 0.8 MPa. The stress ratio is also divided into the following categories: the low stress ratio is less than or equal to 4%, and the high stress ratio is greater than 4%. Data points in Figure 11a are classified and analyzed; a probability ratio of 77.2% occurred for low-incidence stress corresponding to a low stress ratio, and a probability ratio of 95.4% occurred for high-incidence stress corresponding to a high stress ratio.
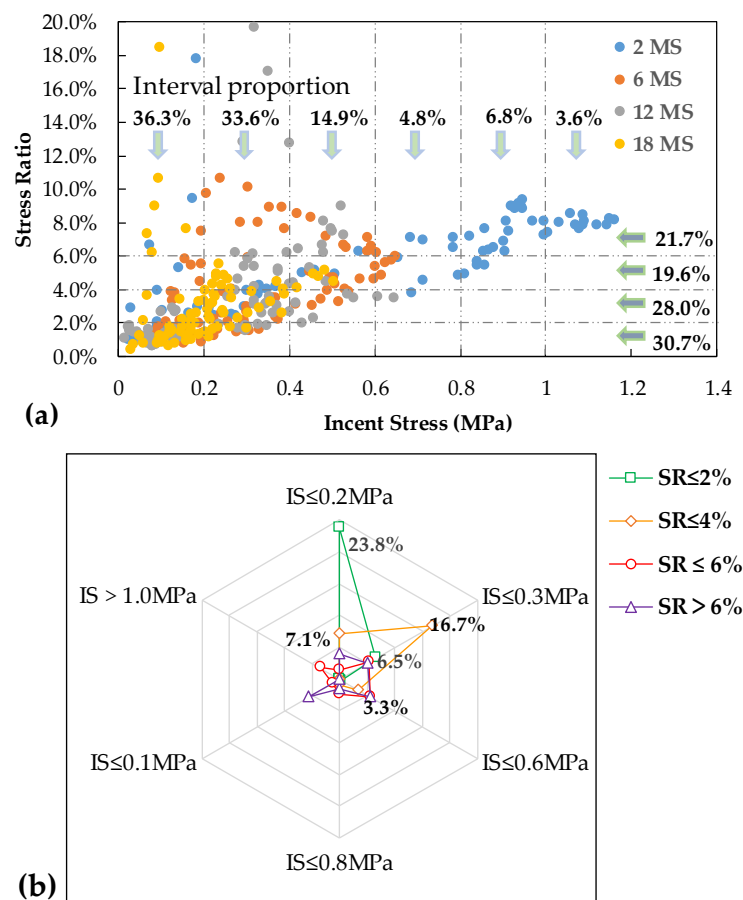
Figure 11. Distribution characteristics of the stress ratio: (**a**) stress ratio data points distribution under different incident stresses; (**b**) statistical distribution of the stress ratio interval under different incident stresses.

In Figure 11b, the first four groups with a high proportion of data points in the total number are:

(a) The incident stress is less than 0.2 MPa, and the stress ratio is less than or equal to 2%, accounting for 23.8%.
(b) The incident stress is less than 0.3 MPa, and the stress ratio is less than 4%, accounting for 16.7%.
(c) The incident stress is less than 0.3 MPa, and the stress ratio is less than 4%, accounting for 7.1%.
(d) The incident stress is less than 0.2 MPa, and the stress ratio is less than 2%, accounting for 6.5%.

The above four categories account for 54.2% of the total data points. The results above show that the incident stress is positively correlated with the stress ratio, i.e., the greater the incident stress, the greater the incident ratio.

4.4. Discussion

(1) The CPB materials deformation before uniaxial strain failure can reach up to 2–5% according to the literature [56,61,62], and the UCS of CPB materials usually does not exceed 10 MPa, while the UCS ranges of CPB required for the mining method are generally 2–5 MPa, and the ratio of the peak pressure strength of a higher strain rate to static is about 2.0, according to [63]. Therefore, compared with rock or high-strength concrete materials, the sensitivity fluctuation range of the HJC model parameters is not obvious. The sensitive parameters such as *A*, *B*, and *N* can be obtained from UCS and CTC tests in the lab. The HJC material model is used to simulate CPB material,

the UCS and CTC were carried out, and the yield surface parameters of the HJC model based on the test results are calculated in the present work.

(2)   A path on the ore and CPB contact surface of the ore and CPB stope is set, which is the collection of CPB elements closest to the explosion source. Theoretically, the stress of the CPB element is the maximum value of the corresponding elevation on the path. By comparing the stress relationship between the elements on both sides of the CPB and the ore at the observation point, the blasting effect of four-layer blasting is studied. It can be seen that the stress difference between layers is very small, and there is no obvious cumulative effect, which may be related to the low explosive charge.

(3)   Order-sequence blasting is adopted instead of time-sequence blasting for layered lift blasts. This is because the initial element stress and node velocity of the next blasting are the results of the previous sequential blasting for time-sequence blasting, so the layered blasting is relatively continuous. However, the node velocity of the previous blasting is reset to zero for each blast, and the elements stress and deformation of the previous blasting are reserved for the next layered blasting for order-sequence blasting; thus, the stress state between the stages is no longer continuous, which is much closer to the actual situation of layered blasting.

(4)   The maximum principal stress of the CPB on the interface side is more than 10 MPa according to the literature [36], which is higher than 1.2 MPa, the highest record in this paper. The main reason for this is that the charge density and charge mount differ. For example, three rows of blast holes are set within 5 m, and the explosives in the holes are detonated at the same time as they are in the literature. This model adopts single-hole blasting, with a blast-layered height of 6 m, and the geometric parameters set in this study are close to the actual mine, with an external row spacing of about 2 m. The charge density, explosive properties, and rock properties are also as close to the typical mines as possible. It is not very accurate to predict the blasting effect under actual working conditions. It is reasonable to believe that, with the increase in blasting holes or the increase in the number of explosives in one blasting hole, the incident stress is bound to increase.

(5)   The horizontal stress induced by the adjacent blast is far greater than that under the static pressure model in the CPB stope, and the obvious extensile area is also opposite to the static analysis model, which provides a reference for the stability analysis of the CPB stope under similar working conditions.

5. Conclusions

In conclusion, a layered lift blast in a primary stope is simulated in this study; the burden size, explosive charge, and ore and CPB materials properties are also within the range of typical mines. Single-hole layered blasting is selected to study the propagation law of stress waves at the interface. However, due to the influence of the explosive charge weight, the incident stress may be less than the actual values. It is reasonable to believe that, with the increase in the number of blast holes or the charge weight, the incident stress will inevitably increase, and the plastic damage zone in the CPB stope will also expand accordingly. A 1/4 numerical analysis model with dimensions of 8 m × 2 m × 24 m (L × W× H) was established in the present work, a two-step mining process including the primary CPB stope and the secondary ore stope was simulated, the secondary ore stope was mined out by four layered lift blasts, each layer was set to 6 m equally, an analysis of the numerical calculation results of the layered lift blast was carried out, and the following conclusions were obtained:

(1)   The CPB stope in the range within the height of the explosive charge was dominated by horizontal compressive stress, and tensile stress was generated in the area above the blasting charge height, while the mined section under the charge height has no obvious blasting impact.

(2)   The maximum incident compressive stress is close to 1.3 MPa and occurs in the area closest to the explosion source. The maximum induced tensile stress occurs in the range above the charge height, which is about 0.2 MPa.

(3) The stress ratios of the four-layered lift blasts are 3.6%, 3.8%, 4.0%, and 4.8%, respectively, and the stress ratios increase slightly with the increase in the blast sequence.

(4) The incident stress is positively correlated with the stress ratio, i.e., the greater the incident stress, the greater the incident ratio.

(5) The incident stress at the initial stage of blasting (about 2 MS) is the maximum, which is about 0.6~1.3 MPa, and the corresponding stress ratio is in the range of 4%~10%. The stress decreases after the peak impact stress (after 2 MS), and the corresponding incident stress ratio also decreases to less than 6%.

Author Contributions: Conceptualization, Z.L. and Y.Z.; methodology, Z.L.; software, Z.L.; validation, X.P. and W.X.; formal analysis, Z.L.; investigation, Z.L.; resources, L.G.; data curation, W.X.; writing—original draft preparation, Z.L.; writing—review and editing, Z.L.; visualization, Y.Z.; supervision, B.Y.; project administration, L.G.; funding acquisition, B.Y. All authors have read and agreed to the published version of the manuscript.

Data Availability Statement: The original contributions presented in the study are included in the article, and further inquiries can be directed to the corresponding authors.

References

1. Cano, Á.; Kunz, N.C. Large-scale and small-scale mining in Peru: Exploring the interface. *Resour. Policy* **2022**, *76*, 102530. [CrossRef]
2. Pengyu, Y.; Li, L. Investigation of the short-term stress distribution in stopes and drifts backfilled with cemented paste backfill. *Int. J. Min. Sci. Technol.* **2015**, *25*, 721–728. [CrossRef]
3. Hustrulid, W.A.; Bullock, R. *Underground Mining Methods: Engineering Fundamentals and International Case Studies*; Society for Mining, Metallurgy, and Exploration: Englewood, CO, USA, 2001.
4. Sivakugan, N.; Rankine, R.M.; Rankine, K.J.; Rankine, K.S. Geotechnical considerations in mine backfilling in Australia. *J. Clean. Prod.* **2006**, *14*, 1168–1175. [CrossRef]
5. Rybak, J.; Kongar-Syuryun, C.; Tyulyaeva, Y.; Khayrutdinov, A.M. Creation of Backfill Materials Based on Industrial Waste. *Minerals* **2021**, *11*, 739. [CrossRef]
6. Thompson, B.; Bawden, W.; Grabinsky, M. In situ measurements of cemented paste backfill at the Cayeli Mine. *Can. Geotech. J.* **2012**, *49*, 755–772. [CrossRef]
7. Nieto, A. *SME Mining Engineering Handbook*, 3rd ed.; Hartman, H.L., Ed.; Society for Mining Metallurgy and Exploration, Inc.: Littleton, CO, USA, 2011; p. 11.
8. Yugo, N.; Shin, W. Analysis of blasting damage in adjacent mining excavations. *J. Rock Mech. Geotech. Eng.* **2015**, *7*, 282–290. [CrossRef]
9. Esmaeili, M.; Tavakoli, B. Finite element method simulation of explosive compaction in saturated loose sandy soils. *Soil Dyn. Earthq. Eng.* **2018**, *116*, 446–459. [CrossRef]
10. Cao, S.; Song, W.; Yilmaz, E. Influence of structural factors on uniaxial compressive strength of cemented tailings backfill. *Constr. Build. Mater.* **2018**, *174*, 190–201. [CrossRef]
11. Li, Z.; Guo, L.; Zhao, Y.; Peng, X.; Kyegyenbai, K. A Particle Size Distribution Model for Tailings in Mine Backfill. *Metals* **2022**, *12*, 594. [CrossRef]
12. Tan, Y.-Y.; Yu, X.; Elmo, D.; Xu, L.-H.; Song, W.-D. Experimental study on dynamic mechanical property of cemented tailings backfill under SHPB impact loading. *Int. J. Miner. Met. Mater.* **2019**, *26*, 404–416. [CrossRef]
13. Wang, Z.; Huang, Y.; Xiong, F. Three-dimensional Numerical Analysis of Blast-induced Damage Characteristics of the Intact and Jointed Rockmass. *Comput. Mater. Contin.* **2019**, *60*, 1189–1206. [CrossRef]
14. Gharehdash, S.; Barzegar, M.; Palymskiy, I.B.; Fomin, P.A. Blast induced fracture modelling using smoothed particle hydrodynamics. *Int. J. Impact Eng.* **2019**, *135*, 103235. [CrossRef]
15. Mohanty, B.; Trivino, L.F. Blast vibration monitoring in cemented paste backfill during its curing stage—A case study. In Proceedings of the Mine Fill 2014: Eleventh International Symposium on Mining with Backfill, Perth, Australia, 20–22 May 2014; pp. 493–501.
16. Singh, P.; Roy, M. Damage to surface structures due to blast vibration. *Int. J. Rock Mech. Min. Sci.* **2010**, *47*, 949–961. [CrossRef]
17. Emad, M.Z.; Mitri, H.; Kelly, C. Effect of blast-induced vibrations on fill failure in vertical block mining with delayed backfill. *Can. Geotech. J.* **2014**, *51*, 975–983. [CrossRef]

18. Duan, Y.; Xiong, D.; Li, G.; Zhang, x. Numerical simulation of disaster effects induced by typical industrial explosive explosion. *J. Henan Polytech. Univ. (Nat. Sci.)* **2011**, *30*, 381–385. [CrossRef]
19. Cheng, D.-S.; Hung, C.-W.; Pi, S.-J. Numerical Simulation of Near-Field Explosion. *J. Appl. Sci. Eng.* **2013**, *16*, 61–67. [CrossRef]
20. Guo, L.; Liu, G.; Qinghai, M.; Chen, X. Research Progress on Mining with Backfill Technology of Underground Metalliferous Mine. *Meitan Xuebao/J. China Coal Soc.* **2022**, *2022*, 1–22. [CrossRef]
21. Hu, J.-H.; Ren, Q.-F.; Yang, D.-J.; Ma, S.-W.; Shang, J.-L.; Ding, X.-T.; Luo, Z.-Q. Cross-scale characteristics of backfill material using NMR and fractal theory. *Trans. Nonferrous Met. Soc. China* **2020**, *30*, 1347–1363. [CrossRef]
22. Centrifuge model studies of fill pressures on temporary bulkheads: Mitchell, R J CIM BullV85, N960, May 1992, P48–54. *Int. J. Rock Mech. Min. Sci. Géoméch. Abstr.* **1993**, *30*, A45. Available online: https://www.sciencedirect.com/science/article/abs/pii/014890629390520N?via%3Dihub (accessed on 16 December 2022). [CrossRef]
23. Liu, G.; Li, L.; Yang, X.; Guo, L. Stability analyses of vertically exposed cemented backfill: A revisit to Mitchell's physical model tests. *Int. J. Min. Sci. Technol.* **2016**, *26*, 1135–1144. [CrossRef]
24. Li, L.; Aubertin, M.; Belem, T. Formulation of a three dimensional analytical solution to evaluate stresses in backfilled vertical narrow openings. *Can. Geotech. J.* **2005**, *42*, 1705–1717. [CrossRef]
25. Li, L.; Aubertin, M. Horizontal pressure on barricades for backfilled stopes. Part I: Fully drained conditions. *Can. Geotech. J.* **2009**, *46*, 37–46. [CrossRef]
26. Li, L.; Aubertin, M. Horizontal pressure on barricades for backfilled stopes. Part II: Submerged conditions. *Can. Geotech. J.* **2009**, *46*, 47–56. [CrossRef]
27. Li, L.; Aubertin, M. A modified solution to assess the required strength of exposed backfill in mine stopes. *Can. Geotech. J.* **2012**, *49*, 994–1002. [CrossRef]
28. Li, L. A new concept of backfill design—Application of wick drains in backfilled stopes. *Int. J. Min. Sci. Technol.* **2013**, *23*, 763–770. [CrossRef]
29. Peng, X.; Guo, L.; Liu, G.; Yang, X.; Chen, X. Experimental Study on Factors Influencing the Strength Distribution of In Situ Cemented Tailings Backfill. *Metals* **2021**, *11*, 2059. [CrossRef]
30. Ainalis, D.; Kaufmann, O.; Tshibangu, J.-P.; Verlinden, O.; Kouroussis, G. Modelling the Source of Blasting for the Numerical Simulation of Blast-Induced Ground Vibrations: A Review. *Rock Mech. Rock Eng.* **2016**, *50*, 171–193. [CrossRef]
31. Cui, L.; Fall, M. Modeling of pressure on retaining structures for underground fill mass. *Tunn. Undergr. Space Technol.* **2017**, *69*, 94–107. [CrossRef]
32. Dobrzycki, P.; Ivannikov, A.L.; Rybak, J.; Shkodkina, V.O.; Tyulyaeva, Y. The impact of Rapid Impulse Compaction (RIC) of large non-cohesive material deposits on the surrounding area. *IOP Conf. Ser. Earth Environ. Sci.* **2019**, *362*, 012132. [CrossRef]
33. Busch, C.L.; Aimone-Martin, C.T.; Tarefder, R.A. Experimental Evaluation of Cratering and Ground Vibration in Clay Soils Subjected to Airblast Loading. In Proceedings of the Geo-Hubei 2014 International Conference on Sustainable Civil Infrastructure, Yichang, China, 20–22 July 2014. [CrossRef]
34. Emad, M.Z.; Mitri, H.S.; Henning, J.G. Effect of blast vibrations on the stability of cemented rockfill. *Int. J. Min. Reclam. Environ.* **2012**, *26*, 233–243. [CrossRef]
35. Suazo, G.; Villavicencio, G. Numerical simulation of the blast response of cemented paste backfilled stopes. *Comput. Geotech.* **2018**, *100*, 1–14. [CrossRef]
36. Li, G.; Deng, G.-Z.; Ma, J. Numerical modelling of the response of cemented paste backfill under the blasting of an adjacent ore stope. *Constr. Build. Mater.* **2022**, *343*, 128051. [CrossRef]
37. Mitchell, R.; Olsen, R.; Smith, J. Model studies on cemented tailings used in mine backfill. *Int. J. Rock Mech. Min. Sci. Géoméch. Abstr.* **1983**, *20*, A12. [CrossRef]
38. Yilmaz, E. Stope depth effect on field behaviour and performance of cemented paste backfills. *Int. J. Min. Reclam. Environ.* **2017**, *32*, 273–296. [CrossRef]
39. Dowding, C.; Aimone-Martin, C.; Meins, B.; Hamdi, E. Large structure response to high frequency excitation from rock blasting. *Int. J. Rock Mech. Min. Sci.* **2018**, *111*, 54–63. [CrossRef]
40. Gharehdash, S.; Shen, L.; Gan, Y. Numerical study on mechanical and hydraulic behaviour of blast-induced fractured rock. *Eng. Comput.* **2019**, *36*, 915–929. [CrossRef]
41. Lu, G.; Fall, M.; Cui, L. A multiphysics-viscoplastic cap model for simulating blast response of cemented tailings backfill. *J. Rock Mech. Geotech. Eng.* **2017**, *9*, 551–564. [CrossRef]
42. Xu, P.; Yang, R.; Zuo, J.; Ding, C.; Chen, C.; Guo, Y.; Fang, S.; Zhang, Y. Research progress of the fundamental theory and technology of rock blasting. *Int. J. Miner. Met. Mater.* **2022**, *29*, 705–716. [CrossRef]
43. van Gool, B. *Effects of Blasting on the Stability of Paste Fill Stopes at Cannington Mine*; James Cook University: Townville, Australia, 2007.
44. Wang, Z.; Wang, H.; Wang, J.; Tian, N. Finite element analyses of constitutive models performance in the simulation of blast-induced rock cracks. *Comput. Geotech.* **2021**, *135*, 104172. [CrossRef]
45. Zhao, L. Numerical investigation on the mechanical behaviour of combined backfill-rock structure with KCC model. *Constr. Build. Mater.* **2021**, *283*, 122782. [CrossRef]
46. Kononenko, M.; Khomenko, O. New theory for the rock mass destruction by blasting. *Min. Miner. Deposits* **2021**, *15*, 111–123. [CrossRef]
47. *GB/T 50123-2019*; Standard for Geotechnical Testing Method. MWR (China): Beijing, China, 2019.

48. Záruba, Q. Earth structures engineering. *Eng. Geol.* **1986**, *22*, 384. [CrossRef]
49. Roy, M.; Singh, P.; Sarim, M.; Shekhawat, L. Blast design and vibration control at an underground metal mine for the safety of surface structures. *Int. J. Rock Mech. Min. Sci.* **2016**, *83*, 107–115. [CrossRef]
50. Saharan, M.R.; Mitri, H. Destress Blasting as a Mines Safety Tool: Some Fundamental Challenges for Successful Applications. *Procedia Eng.* **2011**, *26*, 37–47. [CrossRef]
51. Pagé, P.; Li, L.; Yang, P.; Simon, R. Numerical investigation of the stability of a base-exposed sill mat made of cemented backfill. *Int. J. Rock Mech. Min. Sci.* **2019**, *114*, 195–207. [CrossRef]
52. Holmquist, T.J.; Johnson, G.R.; COOK, W.H. A computational constitutive model for concrete subjected to large strains, high strain rates, and high pressures. In Proceedings of the 14th International Symposium on Ballistics, Québec City, QC, Canada, 26–29 September 1993; pp. 591–600.
53. Ren, G.-M.; Wu, H.; Fang, Q.; Kong, X.-Z. Parameters of Holmquist–Johnson–Cook model for high-strength concrete-like materials under projectile impact. *Int. J. Prot. Struct.* **2017**, *8*, 352–367. [CrossRef]
54. Zhang, H.; Li, T.; Wu, S.; Zhang, X.; Gao, W.; Shi, Q. A study of innovative cut blasting for rock roadway excavation based on numerical simulation and field tests. *Tunn. Undergr. Space Technol.* **2021**, *119*, 104233. [CrossRef]
55. Liu, K.; Wu, C.; Li, X.; Li, Q.; Fang, J.; Liu, J. A modified HJC model for improved dynamic response of brittle materials under blasting loads. *Comput. Geotech.* **2020**, *123*, 103584. [CrossRef]
56. Yang, L.; Xu, W.; Yilmaz, E.; Wang, Q.; Qiu, J. A combined experimental and numerical study on the triaxial and dynamic compression behavior of cemented tailings backfill. *Eng. Struct.* **2020**, *219*, 110957. [CrossRef]
57. Bi, C. Calibration of HJC Constitutive Parameters of Huashan Granite and Its Blasting Damage Numerical Simulation. Master's Thesis, Hefei University of Technology, Hefei, China, 2018.
58. Fang, Q.; Kong, X.; Wu, H.; Gong, Z. Deterination of Holmquist-Johnson-Cook Consitiutive Model Parameters of Rock. *Eng. Mech.* **2014**, *31*, 197–204. [CrossRef]
59. Jiang, H.; He, S.; Wang, J. Parameters determination of elasto-plastic damage cap model for concrete materials. *J. Vib. Shock* **2012**, *31*, 8. [CrossRef]
60. Jayasinghe, B.; Thambiratnam, D.; Perera, N.; Jayasooriya, J. Computer simulation of underground blast response of pile in saturated soil. *Comput. Struct.* **2013**, *120*, 86–95. [CrossRef]
61. Zhao, Y.; Soltani, A.; Taheri, A.; Karakus, M.; Deng, A. Application of Slag–Cement and Fly Ash for Strength Development in Cemented Paste Backfills. *Minerals* **2018**, *9*, 22. [CrossRef]
62. Zhao, Y.; Taheri, A.; Soltani, A.; Karakus, M.; Deng, A. Strength Development and Strain Localization Behavior of Cemented Paste Backfills Using Portland Cement and Fly Ash. *Materials* **2019**, *12*, 3282. [CrossRef]
63. Zheng, D. Research on Macro and Meso Mechanical Properties and Failure Evolution Mechanism of Cemented Tailings Backfill under Dynamic Load. Ph.D. Thesis, University of Science and Technology Beijing, Beijing, China, 2022.